JOURNAL OF AIRCRAFT
Vol. 42, No. 3, May–June 2005

Unsteady Computations of Abrupt Wing Stall Using Detached-Eddy Simulation

James R. Forsythe*
U.S. Air Force Academy, Colorado Springs, Colorado 80920
and
Shawn H. Woodson†
U.S. Naval Air Systems Command, Patuxent River, Maryland 20670

Unsteady computational fluid dynamics calculations are presented of the abrupt wing stall phenomenon on the preproduction F/A-18E using detached-eddy simulation. Detached-eddy simulation combines the efficiency of a Reynolds-averaged turbulence model near the wall with the fidelity of large-eddy simulation in separated regions. Because it uses large-eddy simulation in the separated regions, it is capable of predicting the unsteady motions associated with separated flows. Detached-Eddy Simulation has been applied to predict the unsteady shock motion present on the F/A-18E at transonic speeds over several angles of attack. Solution-based grid adaption is used on unstructured grids to improve the resolution in the separated region. Mean flow results are compared to leading Reynolds-averaged models showing improved predictive capability. Unsteady surface pressures are shown to be in good agreement with experimental measurements. The presence of low-frequency pressure oscillations due to shock motion in the current simulations and the experiments motivated a full aircraft calculation, which showed low-frequency high-magnitude rolling moments that could be a significant contributor to the abrupt wing stall phenomenon.

Introduction

DURING envelope expansion flights of the F/A-18E/F in the engineering and manufacturing development phase, the aircraft encountered uncommanded lateral activity, which was labeled wing drop. An extensive resolution process was undertaken by the U.S. Navy and its contractors to resolve this issue. A production solution was developed, which included revising the flight control laws and the incorporation of a porous wing fold fairing to eliminate the wing drop tendencies of the preproduction F/A-18E/F. The wing drop events were traced to an abrupt wing stall (AWS) on either the left or right wing panel, causing a sudden and severe rolloff in the direction of the stalled wing. An important distinction between wing drop and AWS is that wing drop is the dynamic response of an aircraft to an aerodynamic event, whereas AWS is an aerodynamic event that can trigger a wing drop.[1]

Unsteady measurements on a model of a preproduction F/A-18E were made by Schuster and Byrd,[2] motivated by the following statement: "Since AWS and the resulting lateral instabilities are dynamic or, at best highly sensitive quasi-static phenomena, measurement of unsteady wing surface pressures, loads, and accelerations were incorporated into the test procedures to investigate the potential unsteady causes and/or indicators of AWS." The initial findings from these tests showed highly unsteady surface pressures indicative of shock oscillation.

Although Reynolds-averaged Navier–Stokes (RANS) computational fluid dynamics (CFD) calculations were fairly successful in predicting mean flow characteristics indicative of AWS (see Ref. 3), they failed to predict unsteady shock oscillations even when run time accurate. The turbulence models employed in RANS methods attempt to model the entire spectrum of turbulent motions. Although unsteady RANS (URANS) is sometimes able to capture unsteady effects, often it is not. For example, URANS on a two-dimensional forebody shape contained low-frequency spanswise fluctuations, with greatly improved results over steady RANS.[4] However, for the flow behind an axisymmetric base at supersonic speeds, RANS failed to go unsteady.[5] The most likely reason that URANS failed to provide unsteady shock oscillations for the current flow is the RANS approach itself. Although often adequate in steady flows with no regions of reversed flow, or possibly exhibiting shallow separations, it appears inevitable that RANS turbulence models are unable to predict accurately phenomena dominating flows characterized by massive separations. Unsteady massively separated flows are characterized by geometry-dependent and three-dimensional turbulent eddies, which unsteady RANS may or may not be able to reproduce.

To overcome the deficiencies of RANS models for predicting massively separated flows, Spalart et al.[6] proposed detached-eddy simulation (DES) with the objective of developing a numerically feasible and accurate approach combining the most favorable elements of RANS models and large-eddy simulation (LES). The primary advantage of DES is that it can be applied at high Reynolds numbers as can Reynolds-averaged techniques, but also it resolves geometry-dependent, unsteady three-dimensional turbulent motions as in LES. The initial applications of DES were favorable[7–9] and formed the main motivation for application to AWS.

Unsteady shock oscillations have been highlighted by Dolling[10] as a problem for steady-state methods. The supersonic separated compression ramp pulses at low frequency. The resulting time-averaged surface pressures are smeared due the time averaging of a moving shock. Accurately predicting this flow has eluded CFD researchers for decades. Dolling[10] suggests that better agreement with time-averaged experimental data could be obtained if the CFD simulation included the global unsteadiness of the shock motion, then took a time average. This is the approach that is taken in the current research.

Besides obtaining an improved time-averaged prediction, however, it is also desired to complement unsteady wind-tunnel methods[2] with CFD to gain further insight into the potential of the unsteady flow to contribute to the AWS phenomena. The CFD complements the experiments by providing results unaffected by aeroelastic effects and more detailed flow visualizations.

Presented as Paper 2003-0594 at the AIAA 41st Aerospace Sciences Meeting, Reno, NV, 6–9 January 2003; received 7 June 2003; revision received 20 August 2003; accepted for publication 20 August 2003.

*Associate Professor, Department of Aeronautics; currently Cobalt Solutions, LLC. Senior Member AIAA.

†Aerospace Engineer. Associate Fellow AIAA.

The baseline case considered is an 8% model of a preproduction F/A-18E with 10/10/5 deg flaps (leading-edge flaps/trailing-edge flaps/aileron flaps) at Mach 0.9 and no tails. DES calculations are performed on a baseline and adapted grid and compared to unsteady wind-tunnel measurements and RANS models. Although not a comprehensive validation, confidence is built in the DES method for this class of flow.

To obtain approval for releasing this paper to the public, quantitative information has been removed from most vertical scales as per guidelines from the Department of Defense.

Governing Equations and Flow Solver

The commercial unstructured flow solver Cobalt was chosen because of its speed and accuracy. Strang et al.[11] validated the numerical method on a number of problems, including the Spalart–Allmaras model (which forms the core of the DES model). Tomato et al.[12] converted the code from explicit to implicit, enabling Courant–Friedrichs–Lewy (CFL) numbers as high as one million. Grismer et al.[13] then parallelized the code, yielding a linear speedup on as many as 1024 processors. Forsythe et al.[14] provided a comprehensive testing and validation of the RANS models: Spalart–Allmaras, Wilcox's k–ω, and Menter's models. The Parallel METIS (ParMetis) domain decomposition library of Karypis and Kumar[15] and Karypis et al.[16] is also incorporated into Cobalt. ParMetis divides the grid into nearly equally sized zones that are then distributed among the processors.

The numerical method is a cell-centered finite volume approach applicable to arbitrary cell topologies, for example, hexahedrals, prisms, tetrahdra. The spatial operator uses the exact Riemann solver of Gottlieb and Groth,[17] least-squares gradient calculations using QR factorization to provide second-order accuracy in space, and total variation diminishing flux limiters to limit extremes at cell faces. A point implicit method using analytic first-order inviscid and viscous Jacobians is used for advancement of the discretized system. For time-accurate computations, a Newton subiteration scheme is employed, and the method is second-order accurate in time.

The compressible Navier–Stokes equations were solved in an inertial reference frame. To model the effects of turbulence, a turbulent viscosity μ_t is provided by the turbulence model. To obtain k_t (the turbulent thermal conductivity), a turbulent Prandtl number is assumed with the following relation: $Pr_t = c_p \mu_t / k_t = 0.9$. In the governing equations, μ is replaced by $(\mu + \mu_t)$ and k (the thermal conductivity) is replaced by $(k + k_t)$. The laminar viscosity, μ is defined using Sutherland's law.

Reynolds-Averaged Models

To provide a baseline for comparison, computations were performed with two of the leading Reynolds-averaged models. The first model used was the Spalart–Allmaras (S–A) one-equation model.[18] This model solves a single partial differential equation for a variable $\tilde{\nu}$, which is related to the turbulent viscosity. The differential equation is derived by, "using empiricism and arguments of dimensional analysis, Galilean invariance and selected dependence on the molecular viscosity." The model includes a wall destruction term that reduces the turbulent viscosity in the log layer and laminar sublayer and trip terms that provide a smooth transition from laminar to turbulent. For the current research, the trip terms were turned off, and the flow was assumed fully turbulent.

The second model used was Menter's shear stress transport (SST) model.[19,20] The method is a blend of a k–ϵ and a k–ω model, which uses the best features of each model. The model uses a parameter F_1 to switch from k–ω to k–ϵ in the wake region to prevent the model from being sensitive to freestream conditions. The implementation used includes a compressibility correction as detailed in Forsythe et al.[14]

DES

The original DES formulation is based on a modification to the Spalart-Allmaras RANS model[18] such that the model reduces to its RANS formulation near solid surfaces and to a subgrid model away from the wall.[6] The basis is to attempt to take advantage of the usually adequate performance of RANS models in the thin shear layers, where these models are calibrated, and the power of LES for resolution of geometry-dependent and three-dimensional eddies. The DES formulation is obtained by replacing in the S–A model the distance to the nearest wall, d, by $\tilde{d}$, where $\tilde{d}$ is defined as

$$\tilde{d} \equiv \min(d, C_{\mathrm{DES}} \Delta) \tag{1}$$

In Eq. (1), for the computations performed in this project, Δ is the largest distance between the cell center under consideration and the cell center of the neighbors, that is, those cells sharing a face with the cell in question. In natural applications of DES, the wall-parallel grid spacings, for example, streamwise and spanwise, are at least on the order of the boundary-layer thickness and the S–A RANS model is retained throughout the boundary layer, that is, $\tilde{d} = d$. Consequently, prediction of boundary-layer separation is determined in the RANS mode of DES. Away from solid boundaries, the closure is a one-equation model for the subgrid-scale eddy viscosity. When the production and destruction terms of the model are balanced, the length scale $\tilde{d} = C_{\mathrm{DES}} \Delta$ in the LES region yields a Smagorinsky eddy viscosity $\tilde{\nu} \propto S\Delta^2$. Analogous to classical LES, the role of Δ is to allow the energy cascade down to the grid size; roughly, it makes the pseudo-Kolmogorov length scale, based on the eddy viscosity, proportional to the grid spacing. The additional model constant $C_{\mathrm{DES}} = 0.65$ was set in homogeneous turbulence[7] and was used in the following calculations.

Although Strelets,[8] formulated a DES model based on Menter's SST model, the current calculations used only the S–A-based version. This approach was used because the separated region is handled in LES mode and should, therefore, not be too sensitive to the underlying RANS model. S–A-based DES has the advantage that it is one vs two equations and is in general more robust because the gradient of the turbulence model variable is linear aproaching the wall.

Results

Calculation Details

As already mentioned, the configuration examined was an 8%-scale preproduction F/A-18E with 10/10/5 deg flaps set. All of the calculations were carried out on a model with no vertical or horizontal stabilizer (no tails). The force coefficients presented here are compared to a no-tails wind-tunnel model. Wing surface pressures are compared to a wind-tunnel model with tails, however, there was seen to be good agreement in surface wing pressures between a model with tails and that without. The Mach number for all cases was 0.9, with a chord-based Reynolds number of 3.98×10^6. This Reynolds number was set by adjusting the freestream temperature and setting standard day sea level pressure. To compare frequencies and times to unsteady wind-tunnel data, the resulting times in the CFD calculations were scaled by the ratio of the CFD freestream velocity to the wind-tunnel freestream velocity (a factor of 1.28). The wind-tunnel comparisons are from the model tested in the NASA Langley Research Center 16 ft Transonic Tunnel (16TT). The wing was instrumented with both steady and unsteady pressure taps, as shown in Fig. 1. This paper will focus on the G row (highlighted) because it is directly behind the snag (in the streamwise direction), where the shock-induced separated flow occurred farthest forward.

The grids used were unstructured grids created using the tetrahedral grid generator VGRIDns.[21] The Cobalt utility blacksmith was used to recombine the high aspect ratio tetrahedra in the boundary layer into prisms. The Baseline grid was 7.3×10^6 cells for half the aircraft. The average first y^+ for the grid was 0.2 with a geometric growth rate of 1.25. An adapted grid was created in an attempt to improve on poor DES results on the baseline grid at 9-deg angle of attack. The utility (fv2usm) was used to convert the Cobalt solution file to a format readable by RefineMesh, a companion to VGRIDns; see Morton et al.[22] The solution used for adaption was the time-averaged solution from a DES 9-deg angle of attack run. A level of vorticity was selected that contained the separation bubble, and the grid spacing reduced by a factor of 0.6 in each coordinate direction. This should in general lead to $(1/0.6)^3 = 4.63$ times the number of

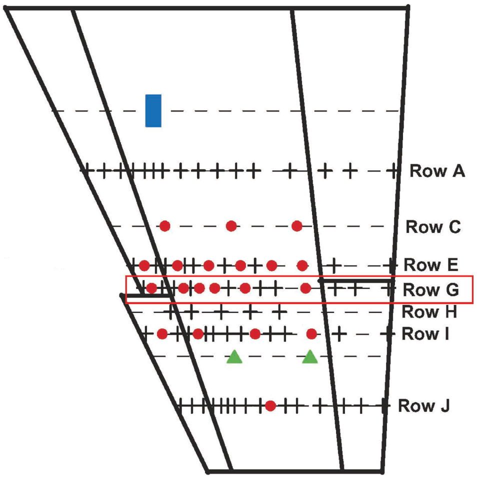

Fig. 1 Experimental pressure ports: ●, unsteady pressure transducer; +, static pressure port; ▮, wing root bending strain gauge; and ▲, outer wing accelerometer.

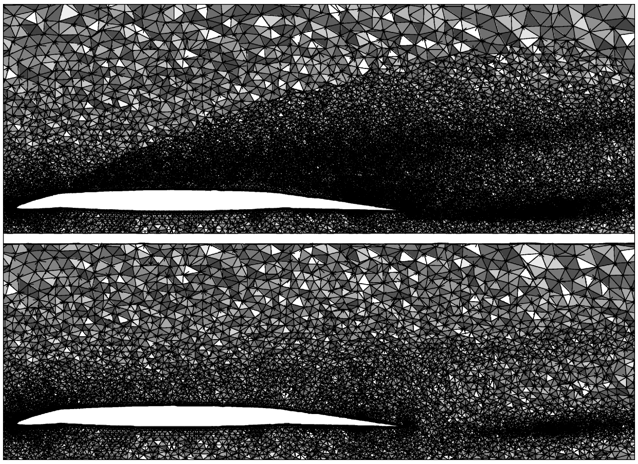

Fig. 2 Baseline vs adapted grid for F/A-18E with no tails.

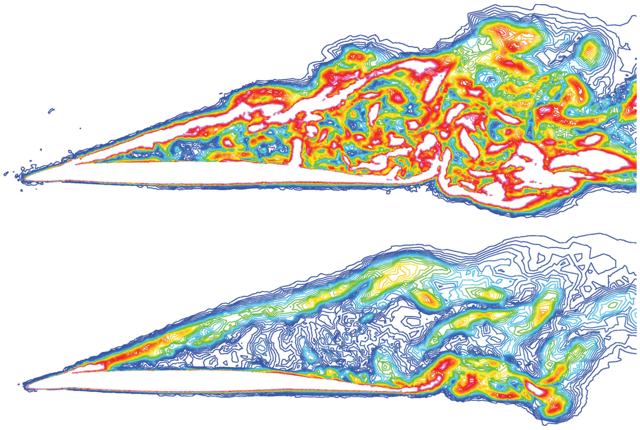

Fig. 3 Vorticy contours on the baseline vs adapted grid for F/A-18E with no tails.

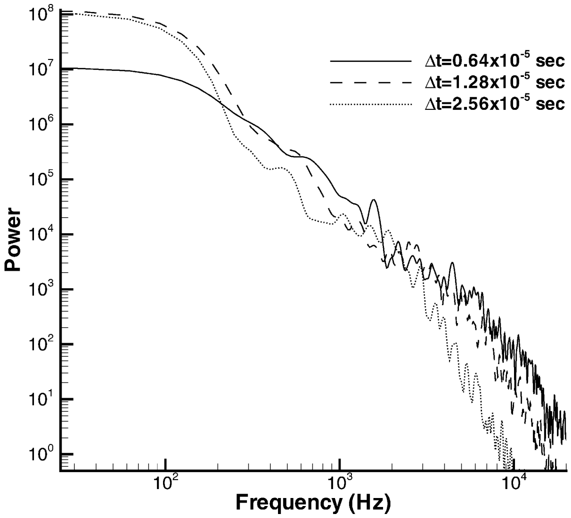

Fig. 4 Power spectral density plot of half-aircraft rolling moment at various timesteps, 9-deg angle of attack.

points. However, because this reduction in spacing was only applied in a narrowly focused region, the grid only increased from 7.3×10^6 to 9.1×10^6 cells. Cross sections of the baseline and adapted grids are shown in Fig. 2. A sample instantaneous DES solution at 9-deg angle of attack is shown in Fig. 3 on the G row. The LES character of DES is clearly shown: As the grid spacing is reduced, smaller and more turbulent length scales are resolved. This reduces the modeling errors by resolving more turbulence, rather than modeling it. When Fig. 2 is compared to Fig. 3, it is also seen that the increased density of points is efficiently placed where needed, in the separation bubble. Although the adaption was carried out at a single angle of attack, the grid was used for the other angles. For lower angles, the separation bubble is farther aft, so that the adapted region included the separation bubble. For angles higher than 9 deg, the separation bubble was larger than the adapted region. The adaption was applied only outside the boundary layer cells. The 9-deg angle of attack case was chose for adaption because this was in the AWS range.

For the RANS calculations, the code was run at a specified maximum global CFL of 1.0×10^6 to accelerate the convergence to steady state. Previous unsteady solutions using RANS models had all failed to obtain any significant levels of unsteadiness. Convergence was assessed by monitoring forces and moments during the run. When the change in forces and moments was less than 1% over 500 iterations, the solution was considered converged. This occurred between 2000 and 4000 iterations depending on the angle of attack.

DES calculations were of course performed time accurate. Three Newton subiterations were used, based on previous experience. To ensure a proper choice in time step, a time step study was performed on the adapted grid. The time steps examined were 0.64×10^{-5}, 1.28×10^{-5}, and 2.56×10^{-5} s. These time steps corresponded to nondimensional (by chord and freestream velocity) time steps of 0.006, 0.012, and 0.024, respectively. The flow was first initialized by running the middle time step for 4000 iterations. Then the calculations were run for 8000, 4000, and 2000 iterations, respectively, over the same length of physical time (0.0512 s). Power spectra of the half-aircraft rolling moment for the three time steps is plotted in Fig. 4. There is fairly poor agreement on the power at the low end of the spectra (below 100 Hz) for the smallest time step. Note, however, that the length of time integrated over is quite small (only able to define 20 Hz), and the low end of the spectra may need longer sampling to define it well. The middle frequency range agrees fairly well for all time steps (between 100 and 2000 Hz). The largest time step starts to fall below the others at 2000 Hz. This represents about 20 iterations per cycle, a reasonable value for a second-order accurate code. The middle time step falls off at about 4000 Hz. This middle time step is used for all of the subsequent calculations. Also note that this spectra provides strong evidence that DES is acting in LES mode because there is a broad range of frequencies resolved and a healthy inertial subrange. For the subsequent DES calculations, the flow was initialized over a time of 0.0512 s, then time averages were taken over at least an additional 0.0512 s.

Steady/Time-Averaged Results

One of the motivating factors behind using a turbulence resolving method such as DES is to provide a more accurate time-averaged solution, mean lift and drag, for example. This has proven true for a

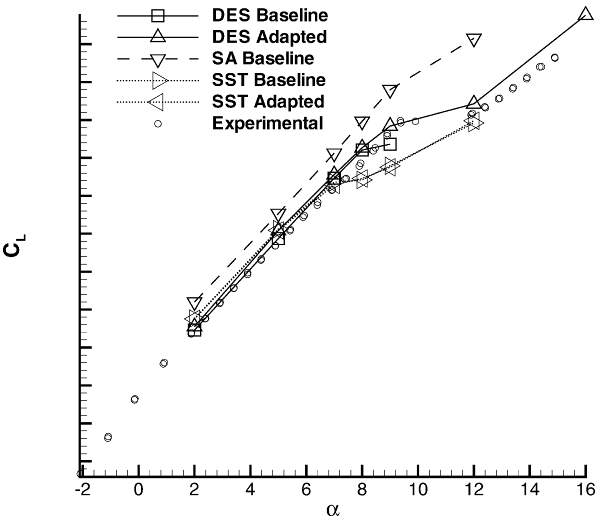

Fig. 5 Lift coefficient vs alpha for the no-tails F/A-18E.

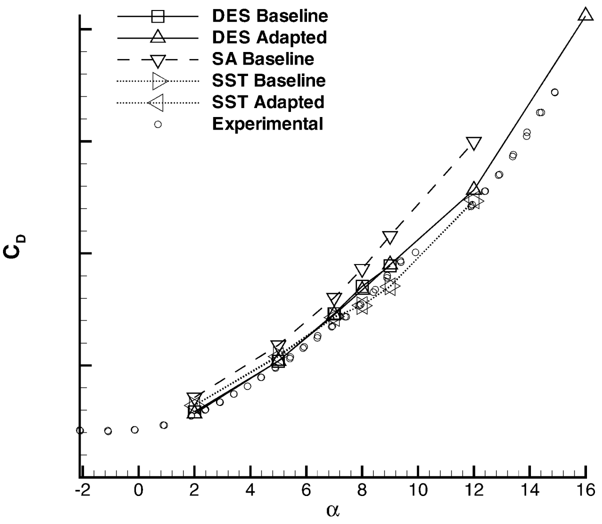

Fig. 6 Drag coefficient vs alpha for the no-tails F/A-18E.

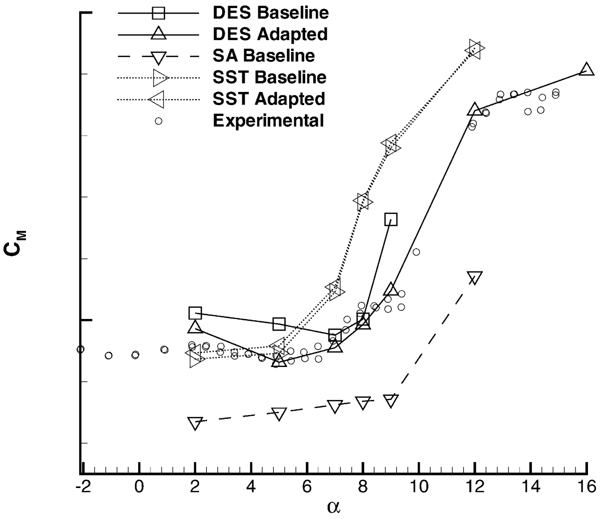

Fig. 7 Pitching moment coefficient vs alpha for the no-tails F/A-18E.

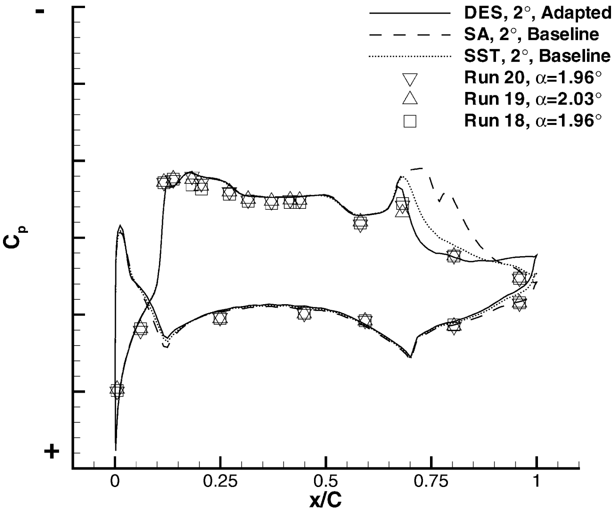

Fig. 8 Time-averaged pressure coefficient vs chord location for the no-tails F/A-18E on the G row, 2-deg angle of attack.

broad range of massively separated flows, such as cylinders, spheres, and airfoils/forebodies/aircraft at high alpha, but has not been examined on a shock-induced separated flow.

Time-averaged-DES lift, drag, and pitching moment coefficients are plotted vs RANS calculations and experimental values in Figs. 5, 6, and 7, respectively. The experimental results were for the same configuration, that is, without tails. The DES on the baseline grid follows the lift curve nicely up until 9 deg, where it drops in lift relative to the experiment. This discrepancy is what prompted the creation of the adapted grid, which matched the experiments more closely. The adapted grid matches the experiments quite well at all angles, with the largest discrepancies at 12 and 16 deg. This slight error could perhaps be removed/reduced by adapting a grid to the flow solution at these angles, because the adapted grid was tailored to 9 deg, which has a smaller separation bubble than the higher angles. The S–A RANS results over predict the lift at all angles, even at the low angles. Parikh and Chung[23] performed S–A calculations on an F/A-18E with the same flap settings and picked up the lift break between 9 and 12 deg, where we do not have calculations. Menter's SST model captures the low angles better, but the lift curve breaks slightly early. SST calculations were performed on both the baseline and adapted grid and showed little sensitivity. Note that grid refinement plays a different role in RANS than in DES. For DES, refining the grid reduces both numerical and modeling errors. In the limit of very fine grids, DES would become direct numerical simulation. For RANS, however, grid refinement reduces only numerical errors, and fixed modeling errors remain. The drag curve (Fig. 6) shows essentially the same trends: overprediction by S–A at all angles, an underprediction by SST near the lift break, and good agreement for the adapted DES.

The pitching moment coefficient (Fig. 7) shows the most sensitivity to the model. Because the current grid has no tails, the moment coefficients are quite different than those presented by Parikh and Chung,[23] which included the empenage. The adapted DES grid shows quite good agreement throughout the entire angle of attack range. S–A underpredicts the moment, whereas SST overpredicts it at all but the two lowest angles.

To understand the differences between the models, pressure coefficients along the G row are plotted vs experiments in Figs. 8, 9, and 10 for 2, 9, and 12 deg, respectively. Figure 8 shows the suggestion that experimentally there is separation over the trailing-edge flap/aileron at 2 deg. Adapted DES does a good job of picking up the pressure level on the aileron correctly, although the agreement at the trailing edge is not perfect (neither is the pitching moment at this angle). SST only slightly underpredicts the pressure, hence, the close but slight overprediction of lift. S–A underpredicts the pressure on the flap by a significant amount, which is likely the cause for the overprediction in lift throughout the low angles of attack.

At 9 deg (Fig. 9), the experiments show a smoothly varying pressure distribution from the snag back to about the half-chord. Schuster and Byrd[2] showed with unsteady pressure measurements that this pressure distribution occurs due to the time averaging of an unsteady shock that moves back and forth over the wing. This is

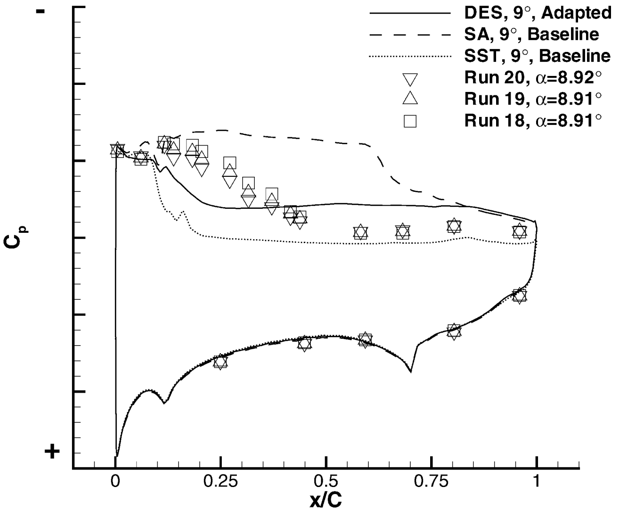

Fig. 9 Time-averaged pressure coefficient vs chord location for the no-tails F/A-18E on the G row, 9-deg angle of attack.

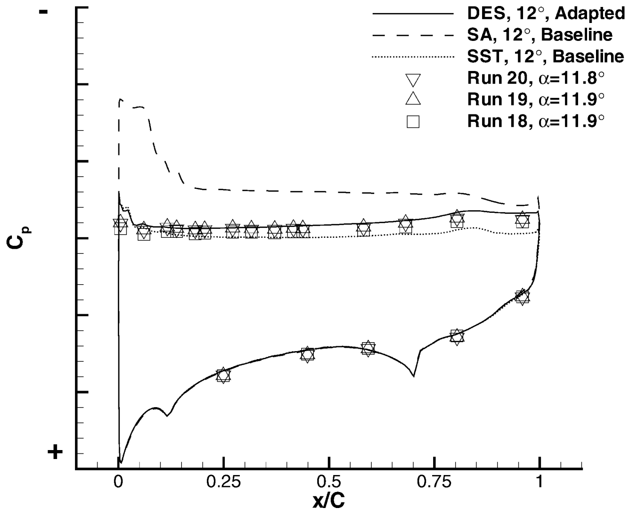

Fig. 10 Time-averaged pressure coefficient vs chord location for the no-tails F/A-18E on the G row, 12-deg angle of attack.

certainly a challenging effect for the RANS approach to model. In this case both S–A and SST predict relatively sharp shocks, with SST separating early, and S–A late. The DES adapted solution, as will be discussed in the following section, contains a moving shock that when time averaged gives a smeared out pressure profile. The time-averaged pressures suggest that the unsteady shock stays too far forward compared to the experiments.

At 12 deg (Fig. 10), the flow is separated over the entire chord from the leading edge of the wing. S–A overpredicts the pressure (and, therefore, the lift), whereas DES and SST match quite well. The fact that SST matches so well here suggests that the errors in pitching moment are arising from a location other than behind the region along the G row.

Unsteady Results

To assess the accuracy of DES in computing unsteady effects associated with AWS, comparisons are made to the unsteady experimental data of Schuster and Byrd.[2] The effect of the unsteady shock on the mean pressure profile is shown in Fig. 11. Figure 11 shows instantaneous pressures at four different times as well as the average pressure for the DES calculation at 9-deg angle of attack. Although the instantaneous shocks are all sharp, when time averaged, a smooth pressure profile results.

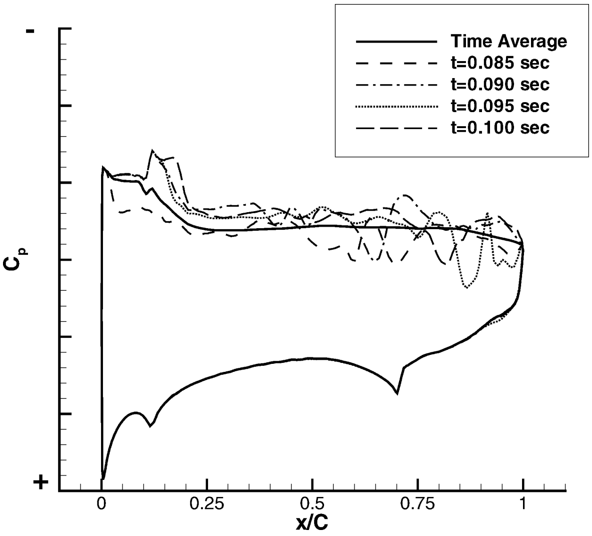

Fig. 11 Pressure contours from the DES adapted calculation at four instants in time and time averaged at 9-deg angle of attack.

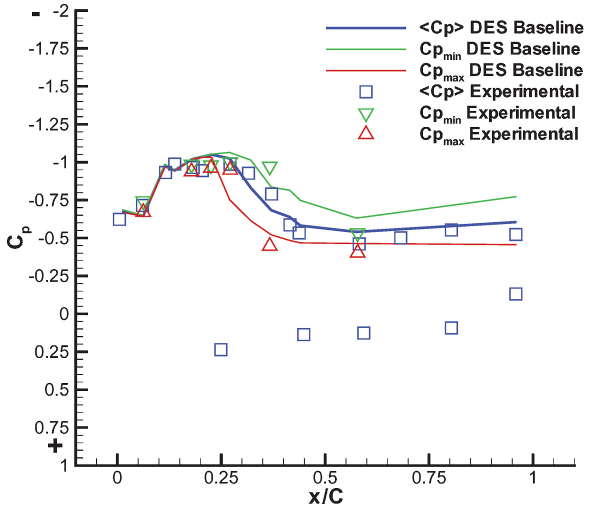

Fig. 12 Minimum, Maximum, and average pressure coefficient on the G row, 7-deg angle of attack.

Comparisons between the DES calculations and the experiments are shown in Figs. 12–14. Surface pressures along the G row are plotted and compared to the experiments, which had 6 unsteady pressure taps and 10 steady taps. Additionally, there were five steady pressure taps on the bottom of the wing. It was impracticable to store the entire set of CFD results for all time steps, and so the CFD calculations were tapped on the G row, and pressures saved every five iterations for subsequent postprocessing. For the baseline calculations, only the 16 experimental taps on the top of the wing were used. For the refined grid calculations, 100 equally spaced points on the G row were tapped on both upper and lower surfaces to allow for more detailed analysis of the shock motion. Pressure statistics were calculated from the experiments and CFD, including the mean, standard deviation, and the minimum and maximum values of pressure. For both the CFD and experiments, any individual pressure that fell outside three standard deviations about the computed mean was excluded for the maximum or minimum pressure value. For the CFD calculations, this mainly smoothed out the minimum and maximum coefficients of pressure behind the shock location.

Statistics at 7 deg are plotted for the baseline grid in Fig. 12. The five experimental mean pressures near the bottom of the plot are from the lower wing surface, where the CFD pressures were not examined. The agreement in the mean, maximum, and minimum pressures on the top surface is quite good. The shock in the CFD prediction is slightly too far forward, and the range of pressure oscillations is slightly underpredicted.

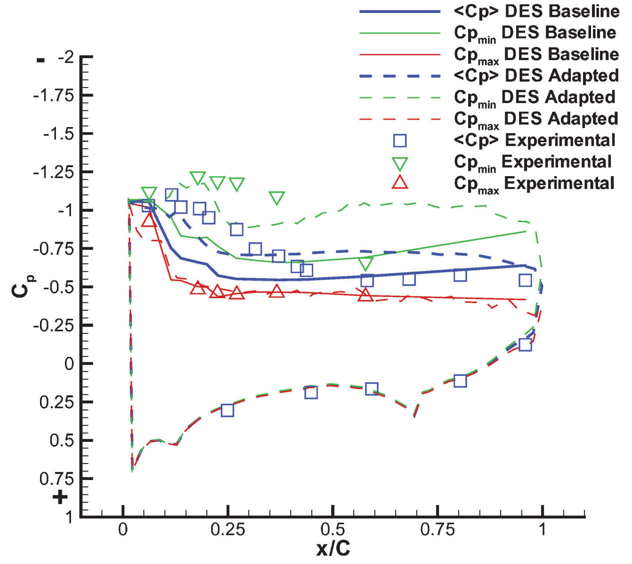

Fig. 13 Minimum, maximum, and average pressure coefficient on the G row, 9-deg angle of attack.

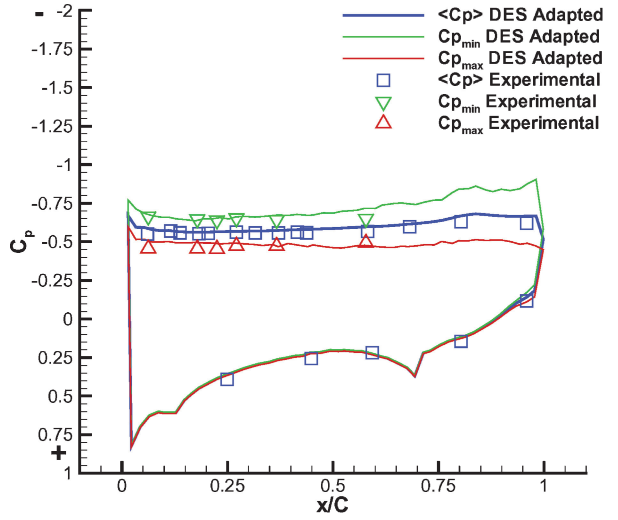

Fig. 14 Minimum, maximum, and average pressure coefficient on the G row, 12-deg angle of attack.

Statistics at 9 deg are plotted for the baseline and adapted grids in Fig. 13. The oscillations in the baseline grid were underpredicted, and the shock is too far forward. The adapted grid helped improve the results, increasing the amount of shock oscillation and moving the mean shock location farther aft. These improvements showed up as an improved mean lift prediction as already discussed.

Statistics at 12 deg are plotted for the adapted grid in Fig. 14. The agreement of the maximum, minimum, and average pressure to the experiments is quite good. The pressures had only a weak oscillation because the flow was fully separated, and there was no shock oscillation as in the 7- and 9-deg cases.

To get a feel for how the frequencies of the CFD shock motions compared to wind-tunnel tests, pressure coefficients were plotted vs time at the six unsteady taps on the G row shown in Fig. 15. The flat low-pressure spots Fig. 15 correspond to times when the shock is aft of that particular spot. Figure 15 indicates that the integration time for the CFD was quite small. The second tap shows that the shock starts off in front of the tap, moves behind it for a short time, then back in front. Therefore, only one shock oscillation is captured in this calculation. This shock oscillation appears to be at a frequency similar to the wind-tunnel results. However, the CFD needs a much longer sampling to provide a useful comparison of frequency content. It appears that the shock never reaches the third through sixth taps in the CFD calculation. For the experiments, the shock reaches as far aft as the fifth tap, but only rarely. This shows that even if the CFD were perfectly matching the physics of the experiment, it may take very long integration times to match time-averaged surface pressure distributions. Thus, there is potential room for improvement in the current calculations by taking longer time averages. The first tap in the CFD calculation has a very strong increase in pressure that was seen visually to be separation off the leading edge of the snag. Although this does not seem to occur in the experiments at this angle, similar events were seen at 9.5 deg (Ref. 2). The higher frequency content in the CFD may simply be due to the higher sampling rate, 15.6 vs 1 kHz.

To determine if unsteady shock oscillation could be a contributor to the AWS phenomenon, half-aircraft rolling moment is examined in Fig. 16. The half-aircraft rolling moment was calculated by taking the rolling moment of the half-aircraft and nondimensionalizing by the span and half the wing area. This of course leads to a nonzero mean coefficient, but a feel for the level of unsteadiness in rolling moment can be obtained by comparing the peak-to-peak differences. The differences in peaks in Fig. 16, although not shown on the axis, was considered significantly large and a potential contributor to triggering an AWS event. A small slice of this rolling moment plot is shown in Fig. 17 with flow visualizations at seven instants in time. Figure 17a corresponds to a large rolling moment because it has low lift, which would produce a right roll. In Fig. 17b, a tiny separation bubble forms on the snag, further reducing lift and increasing the rolling moment. The shock then moves back in Figs. 17c–17e until the lift is at a maximum and the rolling moment is at a minimum. From that point it moves forward in Figs. 17f and 17g.

What is significant is that this shock motion causes a rolling moment change at a low-frequency, approximately 25 Hz. This would scale to 2 Hz for the full-scale aircraft. This was, however, only a half-aircraft calculation, and so care must be taken in drawing conclusions from Fig. 17. The net rolling moment will depend on the flow on the other wing. It would in general be possible for the shock locations on the other wing to be perfectly symmetrical and, therefore, have zero rolling moment. Given the chaotic nature of the flow, however, this seems extremely unlikely. Another possibility is that the shocks on both wings oscillate in a very narrow frequency range, which could give rise to a very low beat frequency. Schuster and Byrd,[2] however, showed that the shock motion occurs in a broadband frequency range so that this would not be expected.

To provide conclusive evidence that the low-frequency shock motion could lead to large low-frequency rolling moments on a full aircraft, the half-aircraft adapted grid was mirrored around the plane of symmetry leading to an 18.2×10^6 cell grid. This grid was then run in the same manner as previous calculations, at 9-deg angle of attack. The resulting rolling moment is shown in Fig. 18, with the same scale as Fig. 16, but centered on zero. The magnitude and frequency of the full-aircraft calculation seems to match up fairly closely to the half-aircraft calculation. The first one-third of the time represents the initial start up of the flow solution and would normally be discarded. However, it is interesting to see that there is a growth of lateral instabilities despite the grid and initial flowfield symmetry. This asymmetry must come from slight asymmetries in the flow solver (asymmetries in the grid partitioning, ordering of the grid, machine roundoff, etc.) that are then amplified by the unstable nature of the flow. If these solver asymmetries were not present, then it would be necessary to provide some flowfield asymmetry in the initial conditions. Comparisons are not made to unsteady rolling moments from the experiments because they were believed to be corrupted by aeroelastic effects because the frequency of rolling moment oscillation correlated with one of the aeroelastic modes of the model, rather than frequencies from the surface pressures. However, the magnitude of the maximum rolling moment of the CFD calculation was similar to that seen in the wind tunnel.

Flow visualizations are also provided for this calculation in Fig. 19, with a zoomed in region of the rolling moment plot. These isosurfaces of zero streamwise velocity are an indicator of the separated region. The shock on the left side starts farther back in Fig. 19a, giving a large positive right rolling moment. As this shock moves

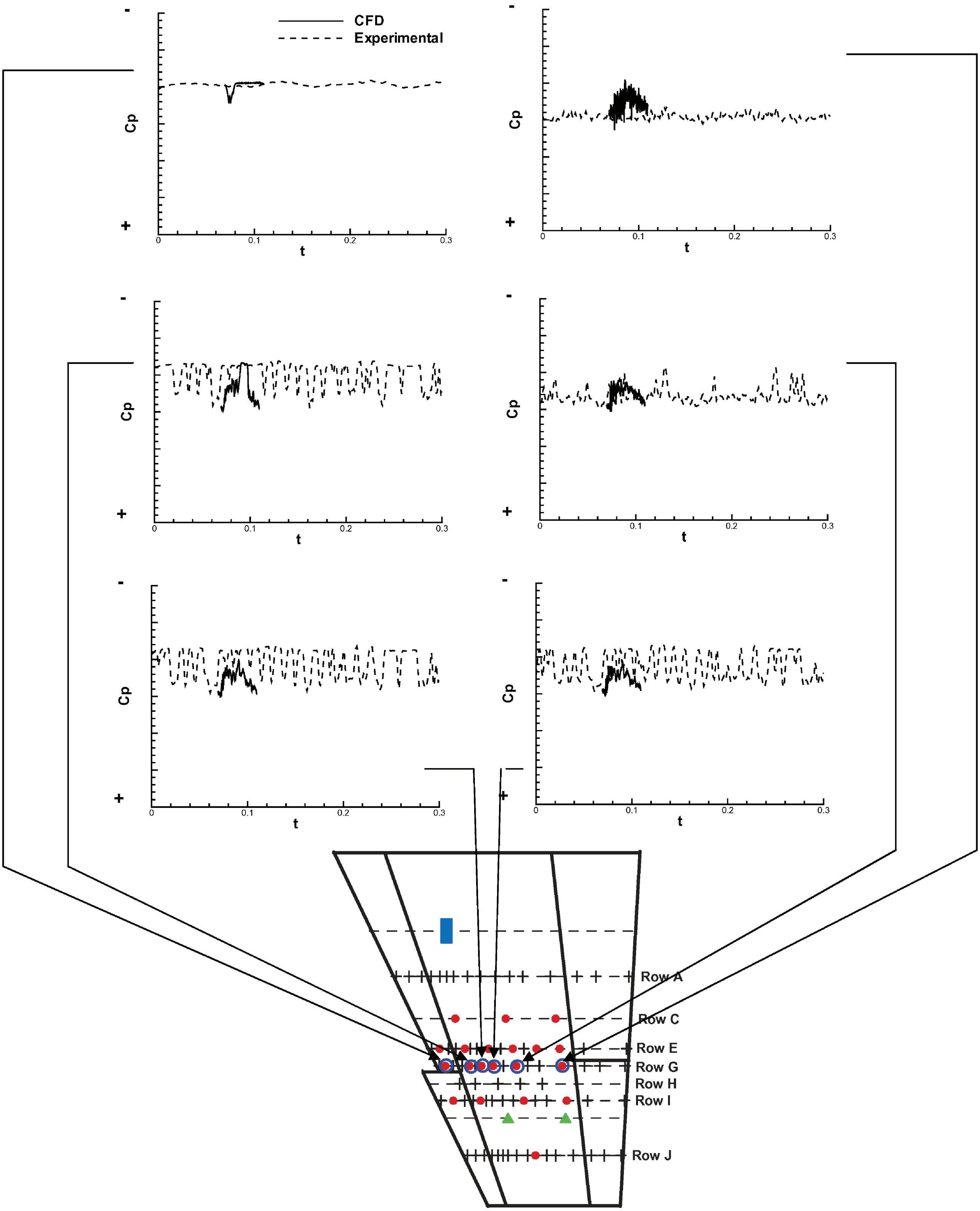

Fig. 15 Pressure coefficient vs time on the G row, experimental vs CFD, 9-deg angle of attack.

forward, the rolling moment moves toward zero in Fig. 19b. Then the right shock moves aft in Fig. 19c, giving a large negative rolling moment.

Comments on the RANS/LES Interface

A potential pitfall (highlighted in the original paper defining DES[6]) for DES occurs if the RANS/LES interface lies deep within the boundary layer. Currently, the location of the interface is determined by the grid, (that is, the position in which $C_{\mathrm{DES}}\Delta = d$). It is possible that grid resolutions may be sufficiently fine that the interface lies within the boundary layer, that is, $C_{\mathrm{DES}}\Delta < \delta$, where δ is the boundary-layer thickness, yet not fine enough to resolve turbulent fluctuations within the boundary layer. For natural applications of DES (as intended in this work), it is desired that the interface be located outside the boundary layer. Location of the interface inside the boundary layer will increase the strength of the destruction term

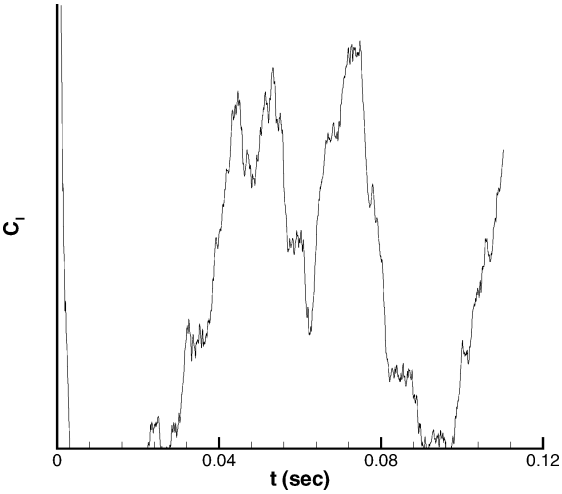

Fig. 16 Rolling moment vs time for half-aircraft calculation (no tails).

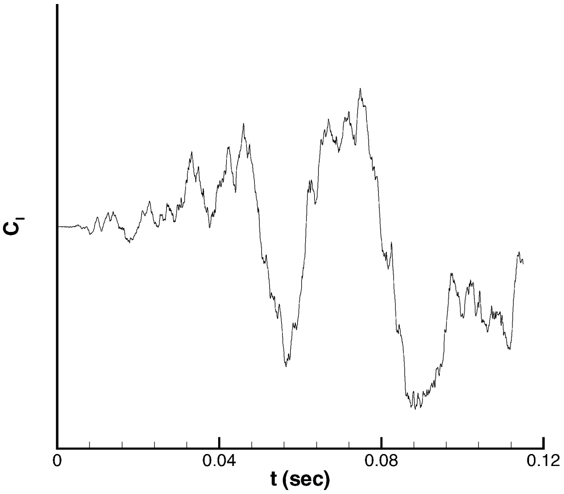

Fig. 18 Rolling moment vs time for full-aircraft calculation (no tails).

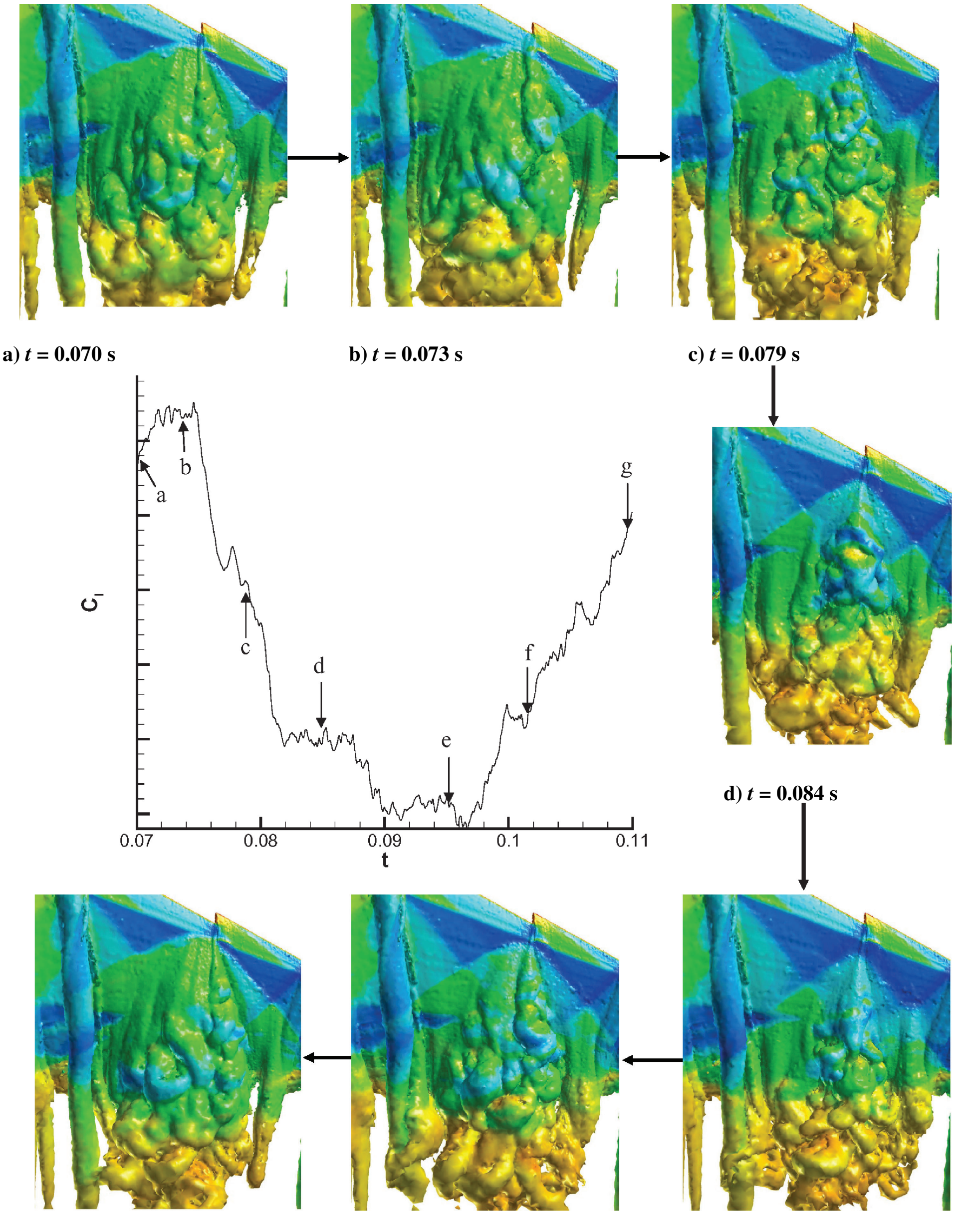

a) *t* = 0.070 s

b) *t* = 0.073 s

c) *t* = 0.079 s

d) *t* = 0.084 s

g) *t* = 0.110 s

f) *t* = 0.102 s

e) *t* = 0.096 s

Fig. 17 Rolling moment vs time and flow visualizations at specific times, half-aircraft; flow visualizations are isosurfaces of vorticity colored by pressure (no tails).

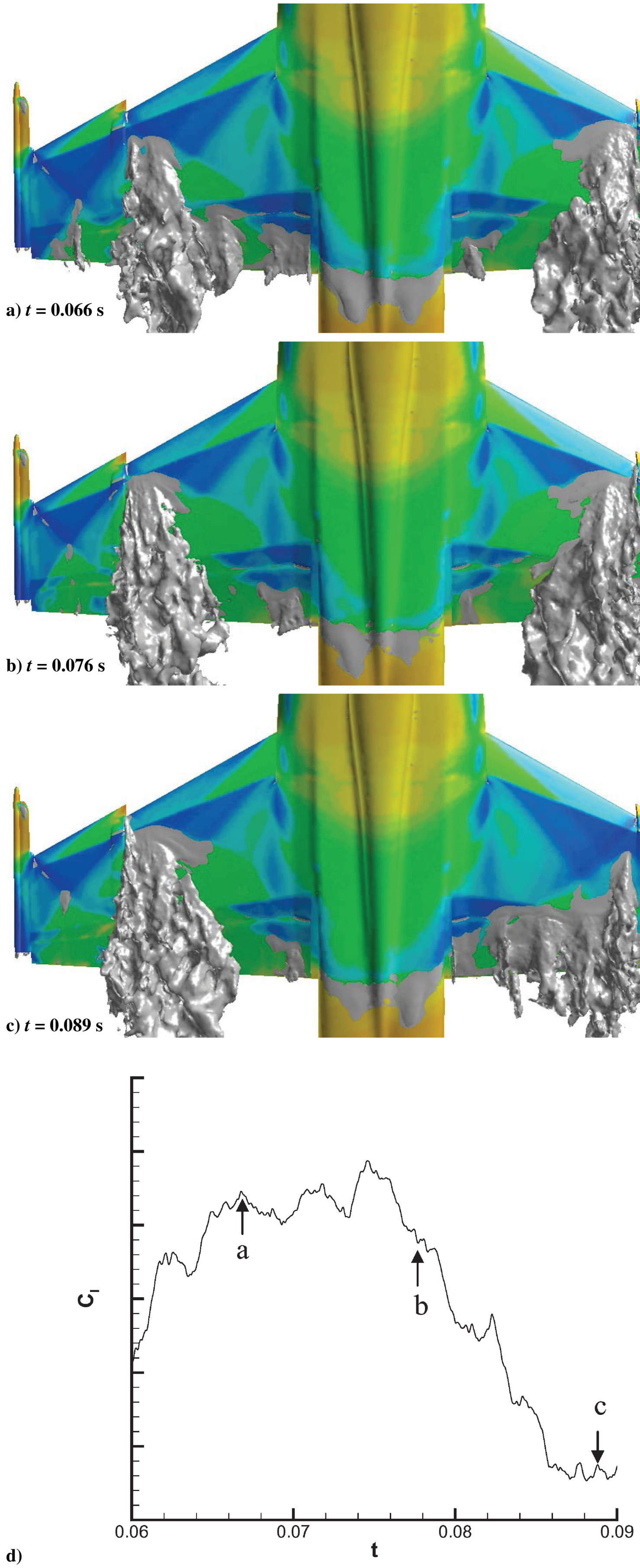

Fig. 19 Rolling moment vs time and flow visualizations at specific times, whole aircraft; flow visualizations are isosurfaces of vorticity colored by pressure (no tails).

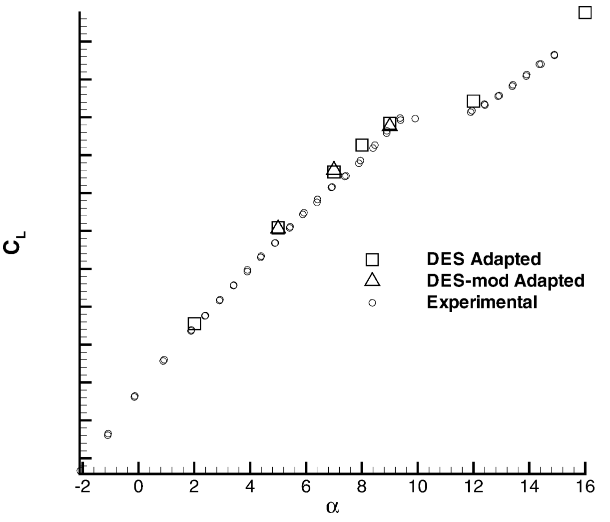

Fig. 20 Lift coefficient vs alpha for the no tails F/A-18E, original and modified DES model.

in the model equation, weakening the eddy viscosity below RANS levels. This could cause reductions in skin friction and earlier separation that in this case would be induced by the grid. Spalart and Allmaras[18] show the destruction term is insignificant in about the upper-half of the boundary layer, and therefore, the most aggressive location of the RANS–LES interface would not be below about half the boundary-layer depth.

For the current application, the interface location was plotted along the G row and compared to the boundary-layer thickness. For the attached case of 2-deg angle of attack, the interface was outside the boundary layer over the first half of the chord. The boundary layer then thickened beyond the interface. By the start of the trailing-edge flap, the interface was at about one-third of the boundary-layer thickness. To determine the effect of this nonideal grid design, several cases were rerun with a modified DES model that retained the wall distance as the length scale if the wall distance was less than the trailing-edge boundary-layer thickness and the original model elsewhere. The resulting time-averaged lift coefficients are plotted in Fig. 20, showing a negligble difference in predictions of the lift. Flow visualizations from the runs using the modified length scale also showed good agreement to the original runs in terms of separation location and shock motion. Although the case was borderline in terms of location of the RANS–LES interface (due to the density of the grid), there seemed to be little ill effect.

The shock separation did occur farther forward with DES than with the S–A RANS model, which could have been caused by grid-induced separation. The lack of sensitivity of the separation location and lift coefficient to the interface location modification, however, makes this unlikely. A more plausible explanation for the difference is the treatment of turbulence in the separated region. The size of the separation bubble can alter the pressure field, altering the pressure gradient and changing the separation location. So despite the fact that RANS treatment is the same in the boundary layer the fact that LES is active in the separation bubble can affect the separation location because of the altered pressure field. This effect is seen on the circular cylinder where RANS and DES give different separation locations.[24] In the present case, the trailing-edge flap at all angles examined had separation, and DES acted in LES mode in that region (outside the boundary layer). This was evidenced by examination of flow visualizations at 2-deg angle of attack. The difference in the resulting pressure field is shown in Fig. 8. For this case the separation location was at the beginning of the trailing-edge flap for both RANS and DES, yet the pressures are significantly different (and improved for DES). Also, note that the separation for the DES calculations occured further aft for the refined grid than the baseline grid at 9-deg angle of attack, which is the opposite effect one would expect from grid-induced separation.

This case highlights that DES must be used with care and the grids designed prudently. Examination of the interface location and boundary-layer thickness during postprocessing should be routine. The grids here were quite dense and, therefore, pushed the limits of the grid design limits of natural applications of DES. Future research in sensing the boundary-layer edge should be pursued to enable the DES model to become more robust to the denser grids that are being more routinely used because of the increase in computer capacity.

Comments on Cost of DES Versus RANS

In deciding whether to use DES or RANS to provide mean flow predictions to look for susceptibility to AWS, the cost must be considered. The DES calculations performed here were about 5–10 times more expensive than a steady RANS calculation because twice the number of Newton subiterations were used, time averages were taken over twice as many iterations, and an adapted grid with about 30% more points was needed. The half-aircraft adapted DES calculations took 9000 CPU-hours on a Compaq ES45. Note that the cost for an URANS calculation would have been the same as a DES calculation; however, URANS failed to go unsteady. At this cost, it may be impracticable to do DES calculations throughout the entire flight envelope. This is especially true because the RANS models were not as accurate, but did at least predict the correct trends in the lift curve break. However, a potential use of DES would be to use RANS to first find the Mach numbers and angles of attack where AWS is suspected. Then DES could be used in focused calculations in these areas. As computer speeds increase, the flight envelope where DES is used could be expanded as its cost is decreased.

Conclusions

In summary, DES calculations were applied to the preproduction F/A-18E with 10/10/5 deg flap set and compared to steady and unsteady experimental measurements and leading RANS models. Comparisons were made to experimental surface pressures (both time averaged and steady) and mean force coefficients. Solution-based adaptation was used to improve the DES calculations, but did not have a significant impact on SST RANS. Unsteady rolling moments were observed on both half- and full-aircraft simulations due to unsteady shock motions.

The mean flow predictions on the adapted grid were seen to be in excellent agreement to the experiments, showing a slight improvement over the SST RANS model and a larger improvement over the S–A RANS model. The improvement seen with grid refinement for DES motivates a more comprehensive grid-refinement study, which would currently be quite costly. The cost of DES was seen to be about 5–10 times higher than steady RANS. It was suggested that steady RANS could be used to find the AWS regime, then focused DES calculations could be performed at a subset of flow conditions.

Comparisons to unsteady pressures built confidence in the accuracy of DES for this class of flow, but highlighted a need for longer time averaging. Current computational speeds put the wind tunnels far ahead in their ability to look at the relatively low-frequency shock oscillation associated with this flow. As computer speeds increase, this gap will naturally narrow. Calculations on both half- and full-span aircraft showed large oscillations in rolling moment at low frequency (close to 2 Hz when scaled to full scale). This supports the conclusion from the unsteady experiments[2]: "This is significant since the combination of large-scale shock motion and low frequency provide a potential triggering mechanism for lateral instabilities, such as wing drop, which probably could not be effectively damped by the automatic flight control system." Because the CFD calculations were for a completely rigid aircraft, there is strong support of the conclusion that "the unsteady aerodynamics experienced on the F/A-18E model at AWS conditions are not a direct result of the structural vibrations encountered in the wind tunnel."[2]

Acknowledgments

The authors wish to express their gratitude to the Office of Naval Research for sponsoring this research. We also gratefully acknowledge the support of Kenneth Wintlzer and William Strang of Cobalt

Solutions for their work on the grid and code, respectively. The authors are also grateful for the advice of Philippe Spalart and Kyle Squires during the project. The advice of the rest of the abrupt wing stall team greatly aided the focus and direction of the work. Finally, the project would not have been possible without the support and CPU hours at the Aeronautical Systems Center/Major Shared Resource Center and the Maui High Performance Computing Center.

References

[1] Hall, R., and Woodson, S., "Introduction to the Abrupt Wing Stall (AWS) Program," *Journal of Aircraft*, Vol. 41, No. 3, 2004, pp. 425–435.

[2] Schuster, D., and Byrd, J., "Transonic Unsteady Aerodynamics of the F/A-18E at Conditions Promoting Abrupt Wing Stall," *Journal of Aircraft*, Vol. 41, No. 3, 2004, pp. 485–492.

[3] Woodson, S. H., Green, B. E., Chung, J. J., Grove, D. V., Parikh, P. C., and Forsythe, J. R., "Understanding Abrupt Wing Stall with Computational Fluid Dynamics," *Journal of Aircraft*, Vol. 42, No. 3, 2005, pp. 578–585.

[4] Squires, K. D., Forsythe, J. R., and Spalart, P. R., "Detached-Eddy Simulation of the separated flow around a forebody cross-section," *Direct and Large-Eddy Simulation IV*, edited by B. J. Geurts, R. Friedrich, and O. Metais, European Research Community on Flow Turbulence and Combustion Series, Vol. 8, Kluwer Academic, Norwell, MA, 2000, pp. 481–500.

[5] Forsythe, J. R., Hoffmann, K. A., Cummings, R. M., and Squires, K. D., "Detached-Eddy Simulation with Compressibility Corrections Applied to a Supersonic Axisymmetric Base Flow," *Journal of Fluids Engineering*, Vol. 124, No. 4, 2002, pp. 911–923.

[6] Spalart, P. R., Jou, W-H., Strelets, M., and Allmaras, S. R., "Comments on the Feasibility of LES for Wings, and on a Hybrid RANS/LES Approach," *Advances in DNS/LES, 1st AFOSR International Conference on DNS/LES*, Greyden Press, Columbus OH, Aug. 1997, pp. 137–148.

[7] Shur, M., Spalart, P. R., Strelets, M., and Travin, A., "Detached-Eddy Simulation of an Airfoil at High Angle of Attack," *Proceedings of the 4th International Symposium on Engineering Turbulence Modelling and Measurements*, edited by W. Rodi and D. Laurence, Elsevier, Amsterdam, May 1999, pp. 669–678.

[8] Strelets, M., "Detached Eddy Simulation of Massively Separated Flows," AIAA Paper 2001-0879, Jan. 2001.

[9] Squires, K. D., Forsythe, J. R., and Spalart, P. R., "Detached-Eddy Simulation of the Separated Flow Around a Forebody Cross-Section," *Direct and Large-Eddy Simulation IV*, edited by B. J. Geurts, R. Friedrich, and O. Metais, European Research Community on Flow Turbulence and Combustion Series, Vol. 8, Kluwer Academic, Norwell, MA, 2001, pp. 481–500.

[10] Dolling, D., "Problems in the Validation of CFD Codes Through Comparison with Experiments," *AGARD Symposium on Theoretical and Experimental Methods in Hybersonic Flows*, CP-514, AGARD, 1993, pp. 19.1–19.15.

[11] Strang, W. Z., Tomaro, R. F., and Grismer, M. J., "The Defining Methods of Cobalt$_{60}$: a Parallel, Implicit, Unstructured Euler/Navier–Stokes Flow Solver," AIAA Paper 99-0786, Jan. 1999.

[12] Tomaro, R. F., Strang, W. Z., and Sankar, L. N., "An Implicit Algorithm for Solving Time Dependent Flows on Unstructured Grids," AIAA Paper 97-0333, Jan. 1997.

[13] Grismer, M. J., Strang, W. Z., Tomaro, R. F., and Witzemman, F. C., "Cobalt: A Parallel, Implicit, Unstructured Euler/Navier–Stokes Solver," *Advances in Engineering Software*, Vol. 29, No. 3–6, 1998, pp. 365–373.

[14] Forsythe, J. R., Strang, W., and Hoffmann, K. A., "Validation of Several Reynolds-Averaged Turbulence Models in a 3D Unstructured Grid Code," AIAA Paper 2000-2552, June 2000.

[15] Karypis, G., and Kumar, V., METIS: Unstructured Graph Partitioning and Sparse Matrix Ordering System, Ver. 2.0, Dept. of Computer Science, Univ. of Minnesota, Minneapolis, MN, July 1997.

[16] Karypis, G., Schloegel, K., and Kumar, V, ParMETIS: Parallel Graph Partitioning and Sparse Matrix Ordering Library, Ver. 1.0, Dept. of Computer Science, Univ. of Minnesota, Minneapolis, MN, July 1997.

[17] Gottlieb, J. J., and Groth, C. P. T., "Assessment of Reimann Solvers for Unsteady One-Dimensional Inviscid Flows of Perfect Gases," *Journal of Computational Physics*, Vol. 78, No. 2, 1988, pp. 437–458.

[18] Spalart, P. R., and Allmaras, S. R., "A One-Equation Turbulence Model for Aerodynamic Flows," *La Recherche Aerospatiale*, Vol. 1, No. 1, 1994, pp. 5–21.

[19] Menter, F. R., "Improved Two-Equation k–ω Turbulence Models for Aerodynamic Flows," NASA-TM-103975, Oct. 1992.

[20] Menter, F. R., "Two-Equation Eddy-Viscosity Turbulence Models for Engineering Applications," *AIAA Journal*, Vol. 32, No. 8, 1994, pp. 1598–1605.

[21] Pirzadeh, S., "Three-Dimensional Unstructured Viscous Grids by the Advancing Layers Method," *AIAA Journal*, Vol. 34, No. 1, pp. 43–49.

[22] Morton, S., Forsythe, J., Cummings, R., and Steenman, M., "DES Grid Resolution Issues for Vortical Flows on a Delta Wing and an F-18C," AIAA Paper 2003-1103, Jan. 2003.

[23] Parikh, P., and Chung, J., "Computational Study of the Abrupt-Wing-Stall Characteristics of F/A-18E and F-16C," *Journal of Aircraft*, Vol. 42, No. 3, 2005, pp. 600–605.

[24] Travin, A., Shur, M., Strelets, M., and Spalart, P., "Detached-Eddy Simulations past a Circular Cylinder," *Flow, Turbulence and Combustion*, Vol. 63, 2001, pp. 293–313.